This article has been accepted for inclusion in a future issue of this journal. Content is final as presented, with the exception of pagination.

Cavity-Membrane-Based Water-Jet Bio-Inspired Thruster With Multidirectional Accelerating Capability

Xinyang Wang, Xuan Pei, Ruixiang Zhu, Taogang Hou, and Xingbang Yang

***Abstract*—Water-jet propulsion helps aquatic creatures achieve both accelerated motion (e.g., flying squid) and long-endurance cruising motion (e.g., jellyfish). That inspired the development of the aquatic unmanned aerial vehicle (AquaUAV) and underwater soft robots. Underwater soft robots achieve water-jet propulsion in all directions but have little propulsion thrust, AquaUAV has large propulsion thrust but can only accelerate from underwater to air. Here, to improve their deficiencies, we proposed a novel water-jet thrusters using cavity-membrane-based water-jet (CM-jet) structure. To quantitatively test the propulsion performance of this novel structure, a tethered prototype as well as a force-pressure measurement system was built. Propulsion theoretical models were developed and refined to explain the propulsion process of CM-jet structure. To explore and verify the propulsion rules, the launch angles α (0°, 15°, 30°, 45°, and 60°) and the initial pressure (0–0.3 MPa) of thruster were varied in the experiments. By combining simulation and experimental results, the thruster using CM-jet structure exhibited propulsion stability independent of launch angles. The maximum net peak thrust is 130 N when $\alpha = 30°$ and $P = 0.3$ MPa. With stable propulsion at any directions, the CM-jet structure may broaden the accelerating directions of water-jet, realizing three translational DoF, which provides a faster propulsion pattern apart from propeller for underwater robot and AquaUAV.**

***Index Terms*—Aquatic unmanned aerial vehicle (AquaUAV), bio-inspired thruster, mantle cavity, water-jet propulsion.**

Manuscript received 16 October 2023; accepted 3 December 2023. Recommended by Technical Editor P. Tallapragada and Senior Editor J. Ueda. This work was supported in part by the National Science Foundation of China under Grant 62103035, in part by Beijing Natural Science Foundation under Grant 3222016, in part by China Postdoctoral Science Foundation under Grant 2021M690337, and in part by the Young Elite Scientists Sponsorship Program by CAST under Grant 2022QNRC001. *(Corresponding authors: Taogang Hou; Xingbang Yang.)*

Xinyang Wang, Xuan Pei, Ruixiang Zhu, and Taogang Hou are with the School of Electronic and Information Engineering, Beijing Jiaotong University, Beijing 100044, China (e-mail: xinyanghhh@buaa.edu.cn; peixuan_mail@163.com; 20120291@bjtu.edu.cn; houtaogang@bjtu.edu.cn).

Xingbang Yang is with the School of Biological Science and Medical Engineering, Beijing Advanced Innovation Centre for Biomedical Engineering, Key Laboratory for Biomechanics and Mechanobiology of Ministry of Education, Beihang University, Beijing 100191, China (e-mail: yangxingbang@buaa.edu.cn).

This article has supplementary material provided by the authors and color versions of one or more figures available at https://doi.org/10.1109/TMECH.2023.3340885.

Digital Object Identifier 10.1109/TMECH.2023.3340885

I. Introduction

WATER-JET propulsion [1], [2] is a widely used propulsion mode by cephalopod mollusks. They use a soft cavity to absorb water and squeeze it to form jet momentum [3]. The jet momentum will generate inverse force on them, thus helping those organisms to achieve forward motion [4]. There are two typical application scenarios. Flying squids [5] take advantage of water-jet propulsion to achieve a rapid ejection from underwater to escape from predators [6]. Jellyfish [7] and scallops [8] move underwater with regular pulsating jets, which is a slow and long-endurance jet pattern [9], [10]. The essence of these locomotion patterns is achieved by squeezing water using a soft cavity.

Inspired by the propulsion pattern of flying squid in Fig. 1, the researchers applied water-jet propulsion to the aquatic unmanned aerial vehicle (AquaUAV) [11], [12], [13]. It is a great challenge to achieve fast underwater takeoff due to the difference in dynamic viscosity and density between water and air. Propeller propulsion in the water–air takeoff process is relatively slow [14], [15], [16], [17]. Therefore, researchers have tried to develop AquaUAV with fast water-jet propulsion capability to achieve rapid underwater takeoff. The authors in [11] and [18] designed a water-jet AquaUAV with takeoff speed of 11 m/s. Chen et al. [19] presented explosion-based water-jet Robobee and the takeoff speed is 2.5 m/s. The authors in [20], [21], and [22] used high-pressure CO_2 as the power source to realize water-jet. The authors in [23] and [24] designed an AquaUAV with consecutive jump-gliding from the water surface and the speed is 10 m/s. Among these prototypes, the water-jet acceleration helps AquaUAV achieve fast flight speed but is utilized only in the takeoff process from underwater to air.

Pulsated jet propulsion [25], [26] handled by jellyfish and octopus, as well as fin propulsion [27], [28] mastered by fish [29], [30] and manta [31], [32], both inspire long-endurance and low-cost locomotion of underwater vehicles [33]. Renda et al. [34] developed a cable-driven underwater soft robot. Its pulsed-jetting propulsion thrust is up to 10.3 N and Serchi et al. [35] optimized the elastic response of this prototype. Then, Serchi et al. [36] proposed a soft hydraulic actuator and its peak thrust

© 2023 The Authors. This work is licensed under a Creative Commons Attribution 4.0 License. For more information, see https://creativecommons.org/licenses/by/4.0/

This article has been accepted for inclusion in a future issue of this journal. Content is final as presented, with the exception of pagination.

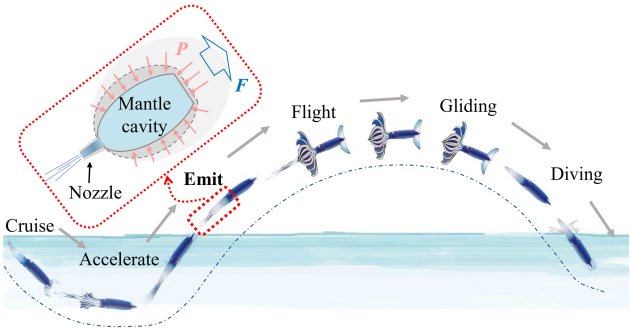

Fig. 1. Aquatic-aerial amphibious locomotion process of the flying squid. Flying squid are accelerated to emit water by squeezing the water through the mantle cavity. The process of squeezing water is specially labeled. The red arrows represent the squeezing pressure P and the propulsion thrust F is generated.

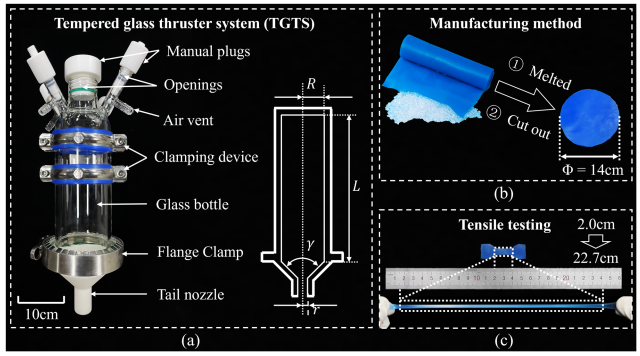

Fig. 3. (a) Tethered TGTS and its parameter schematic sketch. (b) TPR raw materials are melted and the membrane is cut from the TPR materials. (c) Tensile tests are carried out and the membrane has a stretch ratio of 1:8.

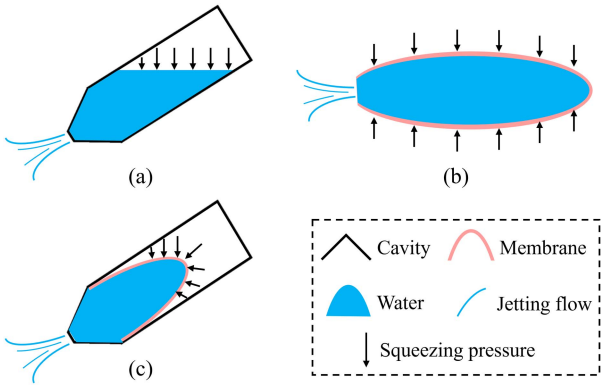

Fig. 2. Conceptual definition diagram of the three water-jet structures. (a) C-jet structure. (b) M-jet structure. (c) CM-jet structure.

can reach about 1 N. Frame et al. [37] developed an untethered soft robotic jellyfish and the thrust can reach about 0.5 N. Robertson et al. [38] presented an underwater water-jet robot and the peak thrust can reach 1 N. Limited by power source, the propulsion thrust of all these prototypes is pretty small, which resulted in slow cruising speed (about 0.05–0.2 m/s). It is worth noting that this water-jet pattern has better motion controllability compared with that used by current AquaUAV and realizes propulsion in all directions. This got us thinking about what would happen if more powerful propulsion was used here.

There are two widely used water-jet structures in Fig. 2(a) and (b), the cavity-based water-jet (C-jet) structure and membrane-based water-jet (M-jet) structure. C-jet structure is widely used by water-jet AquaUAV [11], [20], [23] [see Fig. 2(a)]. The water is stored in the cavity and the volume expansion caused by high-pressure gas or chemical explosion directly squeezes the water [39]. Those high energy source do squeeze water quickly to accelerate. However, for AquaUAV, this accelerating mode is only used in the takeoff process from underwater. M-jet structure is adopted by underwater robots [35], [36], [40] [see Fig. 2(b)]. The ellipsoidal membrane is fixed in the long-axis and the water is squeezed from the short-axis to form the pulsed jet. Compared with the energy source used by C-jet, the M-jet structure cannot get enough energy from existing prototypes, which results in low but stable propulsion thrust.

In this article, we developed a thruster that not only has large propulsion power, but also moves steadily in multiple directions. Based on the high energy source used by C-jet structure and the multidirectional mobility handled by M-jet, here, we propose cavity-membrane-based water-jet (CM-jet) structure for the first time [see Fig. 2(c)]. The membrane is put inside the cavity. The power source squeezes the membrane to produce deformation and membrane squeezes the water out of the nozzle. According to the existing theoretical model [41], [42], [43], [44] and prototype experiments [40], [45], [46], [47], although it can provide stable water-jet in all directions, the propulsion thrust of M-jet structure is little, even far less than its gravity and cannot rapidly realize acceleration motion. Therefore, we will focus on the comparative analysis of simulations and experiments for C-jet and CM-jet structures later.

The rest of this article is organized as follows. In Section II, the tethered prototype as well as force-pressure measurement system was built, and two experimental series were set up for C-jet and CM-jet structures. In Section III, we built two propulsion models for the two structures. In Section IV, the results and phenomena of the model predictions and experiments are presented. In Section V, some possible factors about results are discussed and the three structures were compared. Finally, Section VI concludes this article.

II. Methodology

A. Prototype Design

To facilitate the observation of the flow field changes, a tempered glass thruster system (TGTS) was fabricated and assembled to withstand high pressure. The prototype shown in Fig. 3(a) is the C-jet structure. Its main components include two parts, the tempered glass bottle and the tail nozzle. The physical parameters of each component are listed in Table I. The thruster is made of tempered glass with a wall thickness of 5 mm. The removable tail nozzle is 3-D printed from high-strength

This article has been accepted for inclusion in a future issue of this journal. Content is final as presented, with the exception of pagination.

TABLE I
KEY DESIGN PARAMETERS FOR THE COMPONENTS IN TGTS

Components	Parameter	Value	Unit
Tempered glass thruster	Max. length L	365	mm
	Max. width W	180	mm
	Inner radius R	37.5	mm
	Air outlet radius r_a	5	mm
	Thickness of wall δ	5	mm
Tail nozzle	Retraction angle γ	90	°
	Nozzle radius r	8	mm
	Nozzle length l_n	35	mm
Flange Clamp	Radius R_f	57.5	mm
Overall	Total weight G_t	1974	g
	Total volume V_t	1100	mm^3

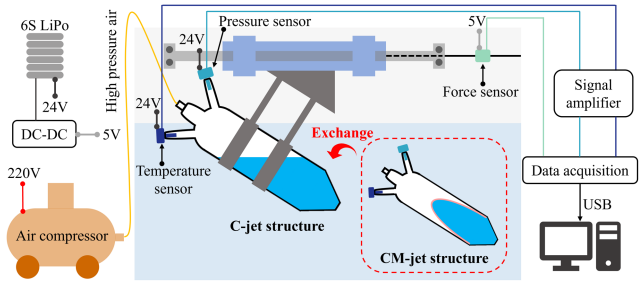

Fig. 4. Control system of the experimental system. This includes electricity supply (6S LiPo, 5 V dc–dc, and 220 V ac), sensors (force sensor and pressure sensor), signal amplifier, data acquisition, and computer. For the mechanical structure, the C-jet structure is fixed under the slide platform and can be replaced by the CM-jet structure.

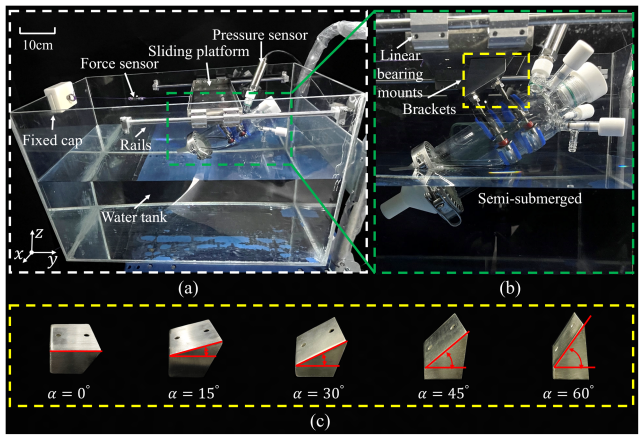

Fig. 5. (a) Force-pressure measurement system. (b) Installation of the TGTS on the sliding platform. (c) Five brackets with different launch angles will be attached between the sliding platform and the TGTS.

photopolymer resin material. Both the tempered glass bottle and the tail nozzle are manufactured with a flange. Thus, the two can be connected by a stainless steel flange clamp and a fluororubber seal. The thruster is then wrapped with three layers of fiberglass tape, which can help thruster withstand an ultimate pressure of 1.5 MPa.

The thruster has five openings at the top end. The size of each of these five openings is controlled by poly tetra fluoroethylene plugs of different sizes. Different sensors can be connected to these openings to obtain physical information inside the bottle, such as pressure and temperature. Two sets of clamping devices made of stainless steel are attached to the outside of the thruster. The clamping devices can be further connected to the force measurement platform.

The CM-jet structure requires the addition of a flexible membrane based on the C-jet structure. In Fig. 3(b), thermo-plastic rubber (TPR) raw materials were melted and cut out to get the membrane. We measured the elongation percent of the TPR material through the tensile testing in Fig. 3(c). By calculating the inner surface area of the tail nozzle in Table I, it is sufficient for membrane deformation to completely squeeze water out if the elongation percent can reach 368%. The dumbbell-shaped sample was stretched from 2.0 to 22.7 cm without any visible breakage or burr on the surface of the sample after being unstretched. TPR material with elongation percent of nearly 1135% is sufficient to provide deformation for the experiment. A circular sample with 14 cm diameter is cut out, which allows for a deformation area of 140 cm^2 around the tail nozzle and retains some protection against breakage. The circle will be placed between the tempered glass bottle and the tab of the tail nozzle. The whole is wrapped by a flange clamp. Thus, the CM-jet structure is completed.

B. Experimental Setup

We developed the experimental system in Fig. 4, a force-pressure measurement system, to quantitatively compare the propulsive performance of C-jet and CM-jet. This system mainly consists of water tank ($80 \times 50 \times 60$ cm^3, made of polymethyl methacrylate), sliding platform, air compressor (volume 30 L and maximum pressure 0.6 MPa), force sensor (Range from -1000 to 1000 N, and resolution 0.01 N), and pressure sensor (Range from -2.5 to 2.5 MPa, and resolution 0.001 MPa), as shown in Fig. 5(a). A pair of smooth and parallel rails are fixed on the two sides of the tank. Sliding platform can slide freely between the two lubricated rails through linear bearing mounts (Product specifications: the dynamic friction factor μ is 0.002). The TGTS is fixed under the sliding platform [see Fig. 5(b)]. These two are connected by bracket (made of stainless steel 304) and the clamping device (made of stainless steel 304). The sliding platform limits the translational DoF of the glass bottle along the z and x directions and only the translational DoF in the y direction, i.e., along the rail, is released. The clamping device restricts the three rotational DoF of the thruster. The force sensor is installed to obtain the propulsion thrust in the y direction and the sampling frequency is 1000 Hz. The water tank, force sensor, and sliding platform are connected by a nonelastic rope. The pressure sensor is fixed in the top opening of thrusters and the sampling frequency is 1000 Hz.

C. Experimental Descriptions

In Table II and Fig. 6, experimental series 1 is designed to measure the propulsion performance of the C-jet structure

This article has been accepted for inclusion in a future issue of this journal. Content is final as presented, with the exception of pagination.

TABLE II
SETTING OF EXPERIMENTAL VARIABLES

	Series 1		Series 2	
Group name	EG 1	MG 1	EG 2	MG 2
With or without membrane	Without		With	
Water volume V_{water} (mL)	350	0	500	150
Pressure range P (MPa)	0 ~ 0.3 (relative pressure)			
Launch angle α (°)	0, 15, 30, 45, 60			
Other variables	All the same			

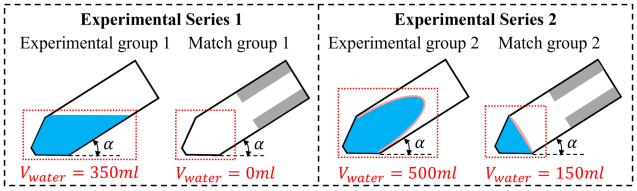

Fig. 6. Difference in water volume V_{water} in two experimental series. In each series, the net water volume obtained by subtracting the MG from the EG is 350 mL. The gray area is a cylinder with a volume of 350 cm^3.

and experimental series 2 is designed to measure the CM-jet structure. The high-pressure gas generated by air compressor is used as the energy source. To obtain large initial pressure, a rubber plug will be inserted into the tail nozzle. Plugs of different sizes, surface roughness, and preload are used to obtain different opening pressures (0–0.3 MPa, relative to atmospheric pressure). Five different brackets are installed to vary the launch angle α, which is 0°, 15°, 30°, 45°, and 60° [see Fig. 5(c)].

The gas escape phase generates underwater air-jet thrust for thruster using C-jet structure and produce "ballooning" phenomenon underwater for thruster using CM-jet structure. These two will result in larger values of water-jet thrust and should be reduced or eliminated (see Fig. 6). Experimental group (EG) obtains the total propulsion thrust (both water-jet and air-jet) and match group (MG) only obtains the propulsion thrust of air-jet. The pure water-jet propulsion thrust, net peak thrust (NPT), can be calculated by differentiating the fitting results of EG from those of MG. Besides, for the water volume, the membrane in the CM-jet structure holds 150 cm^3 volume in its natural unstressed state. To avoid introducing further human operating errors, we set the water volume of 150 mL as initial state for series 2. Also, to maintain a consistent initial air volume in the cavity, a cylinder with 350 cm^3 volume was placed inside the cavity for each match groups. The outer diameter of the cylinder was 37.5 mm, the inner diameter was 21.9 mm, and the length was 120 mm.

Since the dynamic friction factor $\mu = 0.002$, the friction changes in the y direction due to load changes in the z direction can be ignored. The captured thrust and pressure data are displayed in real time and saved on the computer. The thrust data are in the y direction and will be converted to the direction along the axis of the tail nozzle, which is the direction of the launch angle α. Experimental data points will be curve-fitted to investigate the relationship between the variables.

III. PROPULSION MECHANISM

A. Problem Definition

We plot the curve of the gas pressure inside the prototype with time in Fig. 7(a). The air compressor outputs high-pressure gas during $0 \sim t_1$. The heat transfer of the whole process will be neglected [24].

The major difference between C-jet structure and CM-jet is whether the water is in direct contact with the high-pressure gas or not. The water in C-jet structure is directly squeezed by the gas in Fig. 7(b)–(e). Due to gravity, the water surface in the prototype is horizontal naturally. During the air expansion, the air squeezes the upper liquid surface. This part of the water transfers the pressure downward, and the water below is ejected first [see Fig. 7(b)–(d)]. After t_2, the gas pressure decreases rapidly while some water is left [see Fig. 7(e)]. For the CM-jet structure, the gas squeezes the membrane to produce deformation, and the elastic energy stored in the membrane is released. The membrane transfers the displacement and force to the water [see Fig. 7(f)–(i)]. Due to the isotropic material of the membrane, the water will take an ellipsoidal shape under the membrane wrapping. During the air expansion, the squeezing force is distributed perpendicularly with the membrane surface. The water will be squeezed out without being left. The parameters analyzed in the following simulations are mainly based on Table I.

B. Cavity-Based Water-Jet Structure

Different from the existing water-jet propulsion model [39], [48] in which the liquid level is always perpendicular to the nozzle-axis, the C-jet structure here considers the gravitationally actual distribution of liquid inside the water tank [see Fig. 8(a)]. So the launch angle of the prototype is substantial for the propulsion thrust.

According to the impulse theorem, the reaction force F during the jetting is related to the mass m of the water ejected and the flow velocity v of the water, which is

$$F\Delta t = \sum mv. \tag{1}$$

The time of effective water-jet propulsion is t. Differentiate t into n units, and the volume of water ejected in the ith period t_i is V_{w_i}. Since the incompressibility of water, the volume increment of gas expansion in the cavity is also equal to V_{w_i}. The flow velocity v_{w_i} and the mass m_{w_i} satisfy $m_{w_i} = \rho V_{w_i} = \rho A v_{w_i} t_i$, where ρ is the density of water and $A = \pi r^2$ is the cross-sectional area of the tail nozzle. The radius of tail nozzle is $r = 8$ mm. From t_{i-1} to t_i, the whole system should satisfy the conservation of momentum that

$$m_{w_{i-1}} v_{w_{i-1}} + m_{B_{i-1}} v_{B_{i-1}} + m_C v_{i-1} = m_{w_i} v_{w_i} + m_{B_i} v_{B_i} + m_C v_i \tag{2}$$

where $m_{B_{i-1}}$ and m_{B_i} are the masses of water remaining in the system, which satisfy $m_{B_i} = m_{B_{i-1}} - m_{w_i}$. The constant m_C is the mass of TGTS, v_{i-1} and v_i are the velocities of the TGTS. Due to the constant flow of water, the flow rates in each channel

This article has been accepted for inclusion in a future issue of this journal. Content is final as presented, with the exception of pagination.

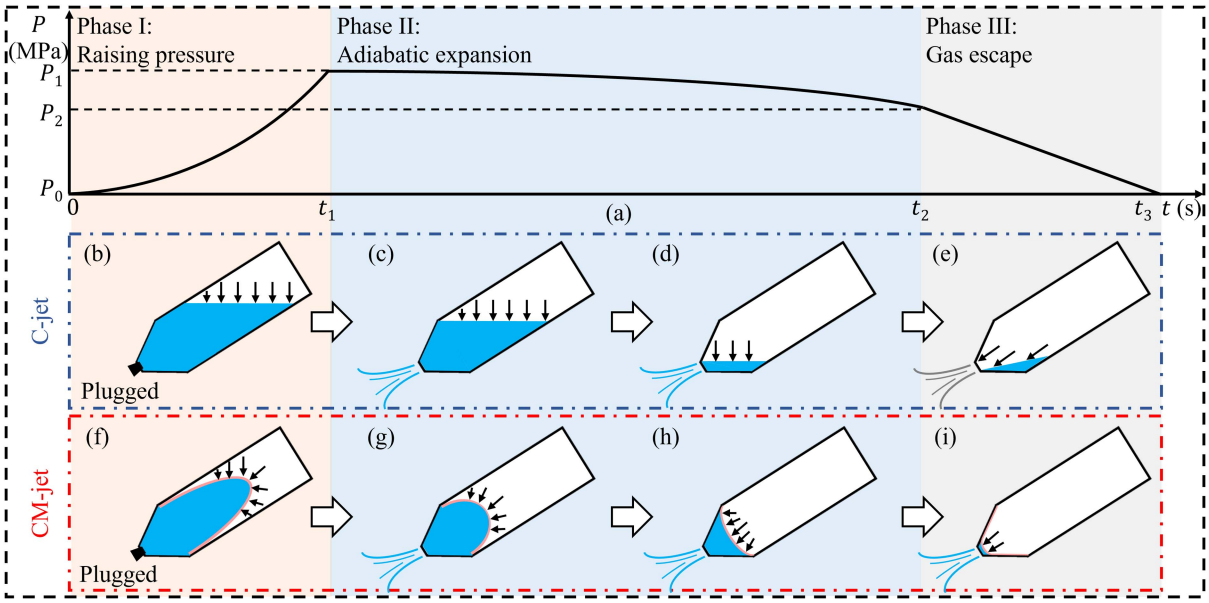

Fig. 7. Ideal water jetting process with the variation of air pressure, which contain the thruster using C-jet structure (blue box) and the thruster using CM-jet structure (red box). (a) Pressure variation with time in the cavity during spraying includes three phases labeled with different background color, i.e., raising pressure, adiabatic expansion, and gas escape. P_0 is the atmospheric pressure and P_1 is the target injection pressure (0–0.3 MPa, relative to atmospheric pressure). (b)–(e) Water-jet process of the thruster using C-jet structure has four stages. The first three stages are to spray water and the last one is to spray gas. (f)–(i) Water-jet process of the thruster using CM-jet structure has four stages and all of them are to spray water. The time on the horizontal axis here is only for illustration and does not represent the actual time of occurrence. During the experiment, $0 \sim t_1$ is about 1 s, $t_1 \sim t_2$ is about 0.2 s, and $t_2 \sim t_3$ is about 0.3 s.

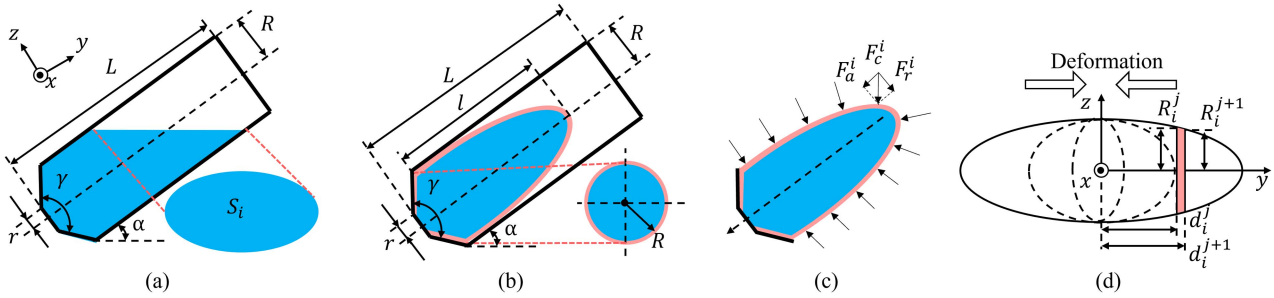

Fig. 8. (a) Physical parameter models of the C-jet structure. (b) Physical parameter models of the CM-jet structure. (c) Air pressure distribution across the membrane and force decomposition. (d) Physical parameters for the discretization of 2-D elliptical models.

section are equal and expressed as

$$\pi R^2 v_{B_{i-1}} = \pi r^2 v_{w_{i-1}} \tag{3}$$

$$\pi R^2 v_{B_i} = \pi r^2 v_{w_i}. \tag{4}$$

According to the kinetic energy theorem, the sum of the work done by the system during t_i will be converted into the increased kinetic energy of the water and the TGTS, that is

$$\sum W_i = \sum E_{K_i} - \sum E_{K_{i-1}} \tag{5}$$

where $\sum W_i$ is the sum of the work done by the system during t_i. $\sum E_{K_i}$ and $\sum E_{K_{i-1}}$ are the total kinetic energy. Each of the them can be expressed as

$$\sum W_i = W_{E_i} + W_{G_i} - W_{\xi_i} - W_{\lambda_i} - W_{D_i} \tag{6}$$

$$\sum E_{K_i} = \frac{1}{2} m_C {v_i}^2 + \frac{1}{2} m_{B_i} {v_{B_i}}^2 + \frac{1}{2} m_{w_i} {v_{w_i}}^2 \tag{7}$$

$$\sum E_{K_{i-1}} = \frac{1}{2} m_C {v_{i-1}}^2 + \frac{1}{2} m_{B_{i-1}} {v_{B_{i-1}}}^2 + \frac{1}{2} m_{w_{i-1}} {v_{w_{i-1}}}^2 \tag{8}$$

where W_{E_i} is the work done by the expansion of the high-pressure gas and expressed as $W_{E_i} = \overline{F_{a_i}} d_i$. During t_i, $\overline{F_{a_i}}$ is the average of the air squeezing force and $\overline{F_{a_i}} = (\overline{P_i} - P_0) S_i$, where $\overline{P_i}$ is the average pressure and expressed as

$$P_i {V_i}^k = P_{i-1} {V_{i-1}}^k \tag{9}$$

$$\overline{P_i} = \frac{P_{i-1} V_{i-1}}{k-1} \left[1 - \left(\frac{P_i}{P_{i-1}} \right)^{\frac{k}{k-1}} \right] / (V_i - V_{i-1}) \tag{10}$$

This article has been accepted for inclusion in a future issue of this journal. Content is final as presented, with the exception of pagination.

where P_i and V_i are the pressure and volumes of air inside the cavity. S_i is the contact area between air and water, which can be expressed by the inner diameter R of the bottle and the launch angle α. d_i is the distance at which the air squeeze does work, which is the height of the liquid surface drops. S_i and d_i satisfy $S_i d_i = V_{w_i}$.

W_{G_i} in (6) is the work done by the gravity of the falling liquid. It satisfies $W_{G_i} = (m_{w_i} + m_{B_i})gd_i$. W_{ξ_i} is the energy loss due to the reduction of the pipe diameter, which is expressed as $W_{\xi_i} = h_{\xi_i}\rho g V_{w_i}$. h_{ξ_i} is the local head loss satisfying (11). ξ is the local head loss coefficient, which is related to the pipe radius ratio $\frac{R}{r}$ and the retraction angle $\gamma = 90°$. W_{λ_i} is the viscous loss caused by the friction between water and the inner wall. W_{λ_i} satisfies $W_{\lambda_i} = h_{\lambda_i}\rho g V_{w_i}$. h_{λ_i} is the frictional head loss and expressed as (12). λ is the frictional head loss coefficient, which is related to the roughness of the inner wall and the Reynolds number Re of the fluid. W_{D_i} is the energy loss due to the drag, including resistance underwater and the friction loss of the sliding platform

$$h_{\xi_i} = \xi \cdot \frac{{v_{w_i}}^2}{2g} \tag{11}$$

$$h_{\lambda_i} = \lambda \cdot \frac{d_i}{2R} \cdot \frac{{v_{w_i}}^2}{2g} \tag{12}$$

$$F_i = m_{w_i} v_{w_i} + m_{B_i} v_{B_i}. \tag{13}$$

Combining (1)–(12), we can obtain the time-dependent thrust F_i in (13). It is worth noting that the volume V_{w_α} remaining in the bottle after jetting can be different under different launch angles α. The volume $V_w - V_{w_\alpha}$ that does the effective work can be obtained experimentally, which is the end point of the integration of (13). When initial volume of water is 350 mL and launch angles α is 0°, 15°, 30°, 45°, and 60°, the remaining volume of water is 350, 141, 39, 11, and 7 mL, respectively.

C. CM-Jet Structure

The CM-jet structure can be regarded as the integration of the C-jet and M-jet structure [see Fig. 8(b)]. The high-pressure gas commonly used by the C-jet structure and the membrane extrusion of the M-jet structure are combined. The entire ellipsoidal structure is placed inside the cavity and the membrane is filled with water. The deformation is characterized by fixing xz plane and varying y axis.

The CM-jet structure satisfies the momentum theorem and the kinetic energy theorem in (1), (2), and (5). Taking into account the presence of membrane, W_i in (5) should be corrected as

$$\sum W_i = W_{E_i} + W_{K_j} + W_{G_i} - W_{\xi_i} - W_{\lambda I_i} - W_{\lambda O_i} - W_{D_i} \tag{14}$$

where W_{E_i} is the work done on the membrane during air expansion. The direction of squeezing F_c is perpendicular to the surface of the membrane. We decompose this force into F_r and F_c, perpendicular to the y axis and parallel to the y axis [see Fig. 8(c)]. The membrane is discretized into q ring-like units in the y axis [see Fig. 8(d)]. For the jth ring-like units, the outer diameter of the ring is R_i^j and the inner diameter is R_i^{j+1}, and the distance from the center are d_i^j and d_i^{j+1}, respectively. For the ellipse with long axis l_i and short axis R, $\frac{{d_i^j}^2}{{l_i}^2} + \frac{{R_i^j}^2}{R^2} = 1$ and $\frac{{d_i^{j+1}}^2}{{l_i}^2} + \frac{{R_i^{j+1}}^2}{R^2} = 1$. The effective work done by the pressure during the period t_i is W_{E_i}

$$W_{E_i} = \sum_{u=0}^{l_i} P_i \cdot \pi \left({R_i^u}^2 - {R_i^{u+1}}^2 \right) \cdot \left(d_i^{u+1} - d_i^u \right) \tag{15}$$

where P_i is the pressure of the air during t_i. According to $PV = nR_rT$, P_i satisfies (9) and (16). P_1 and V_1 are the pressure and volume of the air cavity at the initial state

$$V_i = V_1 + \frac{2}{3}R^2 l - \frac{2}{3}R^2 l_i \tag{16}$$

$$W_{K_i} = \frac{1}{2}k_0 {l_{i+1}}^2 - \frac{1}{2}k_0 {l_i}^2. \tag{17}$$

Besides, W_{K_j} is the value of the change of elastic potential energy [36] during t_i, which is related to the deformation. k_0 is the elastic constant of the membrane and $k_0 = 0.06896$. W_{G_i} is the work done by the gravity. $W_{G_i} = m_{w_i} g(l_i - l_{i+1})\sin\alpha$ and $m_{w_i} = \frac{2}{3}\rho R^2 l_i$. $W_{\lambda I_i}$ and $W_{\lambda O_i}$ are the energy loss due to the friction between water and the inner wall of the membrane as well as the friction between the outer wall of the membrane and the inner wall of the cavity. $W_{\lambda I_i}$ and $W_{\lambda O_i}$ can be neglected in the calculation because the surface of the membrane is extremely smooth after being infiltrated (experimentally: the dynamic friction factor $\mu_m = 0.03$).

The time-dependent thrust F_i during the jetting process can be obtained by combining the (1), (2), and from (13) to (17). V_{w_α} is always 0 because all water is squeezed out by the membrane.

IV. Results

A. Modeling Simulation Results

We perform numerical simulations for two sets of propulsion models constructed in Section III.B and Section III.C. The simulations are solved in MATLAB 2021b under same initial conditions. The initial pressure inside the cavity was 0.2 MPa (relative to atmospheric pressure). The water volume was 350 mL. The launch angle was 45°. The results of the simulation are shown in Fig. 9. The pressure is reduced from 0.2 to 0.07 MPa see Fig. 9(a)]. The thruster using C-jet structure took 190 ms to complete the simulation and has 3 mL water left in the cavity. The thruster using CM-jet took only 140 ms while it can eject all water [see Fig. 9(b)]. That means the water in the CM-jet structure are ejected more quickly, which results in the propulsion thrust of the CM-jet structure throughout the jetting process is always greater than that of the C-jet [see Fig. 9(c)]. The maximum value of the propulsion thrust is 38% higher than that of the C-jet. The former can reach 157 N while the latter is only 113 N.

To demonstrate the rationality of the discretization process in Section III.C, we simulated the flow field in XFlow software in Fig. 9(d). The results show the deformation direction of the membrane and the flow direction of water are consistent with Fig. 8(c) and (d), when the membrane is squeezed by the gas. The

This article has been accepted for inclusion in a future issue of this journal. Content is final as presented, with the exception of pagination.

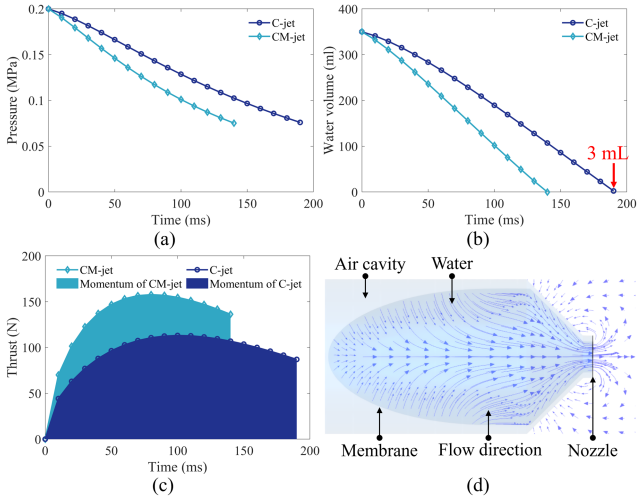

Fig. 9. (a) Trend of pressure inside the cavity over time. (b) Trend of volume of water remaining inside the cavity over time. (c) Trend of thrust generated by thruster using C-jet and CM-jet over time. Shaded area indicates the propulsive momentum. Thruster using CM-jet structure have greater acceleration. (d) Fluid simulation results in XFlow software when the high-pressure air squeezes the membrane in CM-jet structure. Blue arrows indicate the flow direction of the water in the membrane.

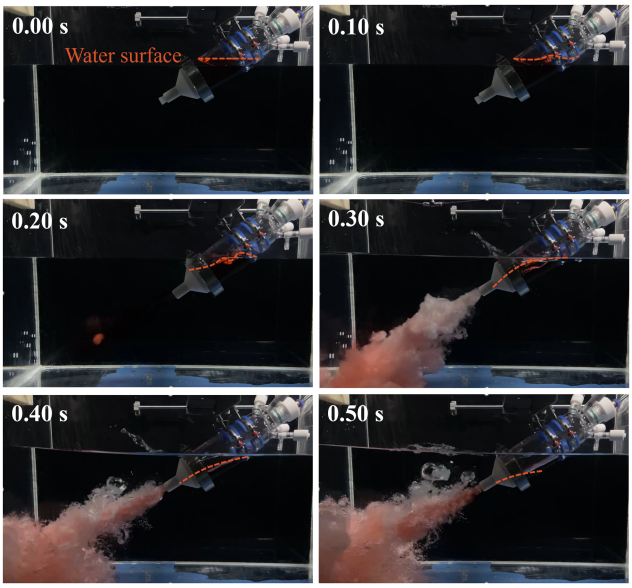

Fig. 10. Water spraying process of the thruster using C-jet structure is recorded at 0.1 s intervals. The jetted water is precolored with a red dye, to distinguish visually. Liquid level of the water is marked with a dashed line.

direction of force and water are perpendicular to the membrane surface and points toward the tail nozzle.

B. Propulsion Performance of C-Jet Structure

Based on the experimental setups in Sections II.B and C, the process of jetting water on the thruster using C-jet structure is filmed in Fig. 10, the experimental results are shown and illustrated in Fig. 11. The initial pressure was varied from 0 to

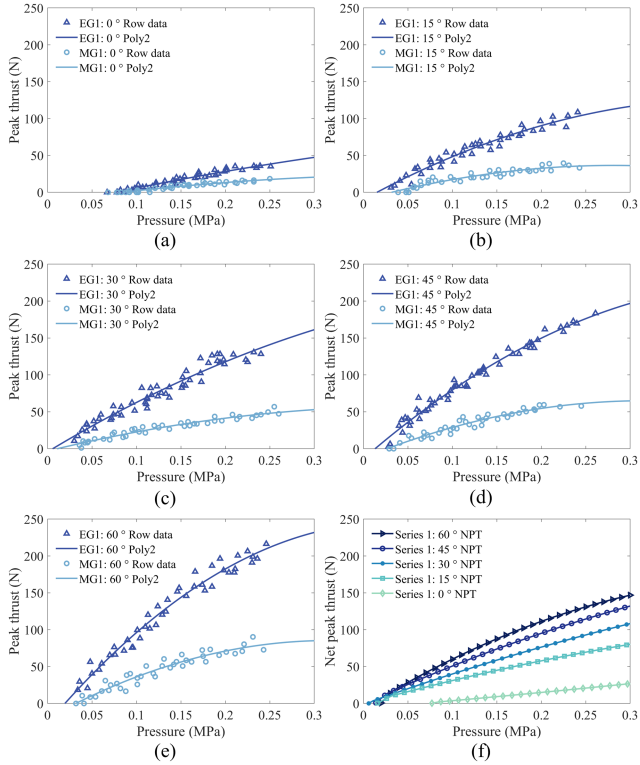

Fig. 11. Experimental results are obtained by completing experimental Series 1 using thruster with C-jet structure. (a)–(e) Results for peak thrust and initial pressure at launch angles α of 0°, 15°, 30°, 45°, and 60°. Peak thrust has been converted to the direction of the nozzle-axis. Both the data scatter and its quadratic polynomial fit curve are shown. Each subplot shows both the results for the EG 1 and MG 1. (f) Five NPT curves are obtained by subtracting the MG 1 fit from the EG 1 fit, based on the previous five sets of fits, respectively.

TABLE III
GOODNESS OF FIT R^2 ABOUT THE PRESSURE-PEAK THRUST FITTING CURVE IN THE EXPERIMENTS

	Series 1		Series 2	
Launch angle	EG 1	MG 1	EG 2	MG 2
0°	0.9446	0.9221	0.9637	0.9359
15°	0.9501	0.8926	0.9701	0.9243
30°	0.9413	0.9397	0.9606	0.9368
45°	0.9807	0.9332	0.9697	0.9030
60°	0.9693	0.9225	0.9704	0.9182

0.3 MPa (relative to atmospheric pressure), and 50 experiments were conducted under five different launch angles (more than 250 total experiments). The R^2 coefficients of quadratic polynomial fitting are given in Table III. From Fig. 11(a)–(e), the numerical curves of both EG 1 and MG 1 shift upward with the increase of launch angle. In Fig. 11(f), the lowest NPT curve of the water-jet is when $\alpha = 0°$. As α increases, the NPT curve shifts upward as a whole. However, the growth rate of the upward shift decreases when increasing in the same launch angle step. The peak propulsion thrust increases as the pressure increases and each curve has a "plateau" period. As the pressure increases, the

This article has been accepted for inclusion in a future issue of this journal. Content is final as presented, with the exception of pagination.

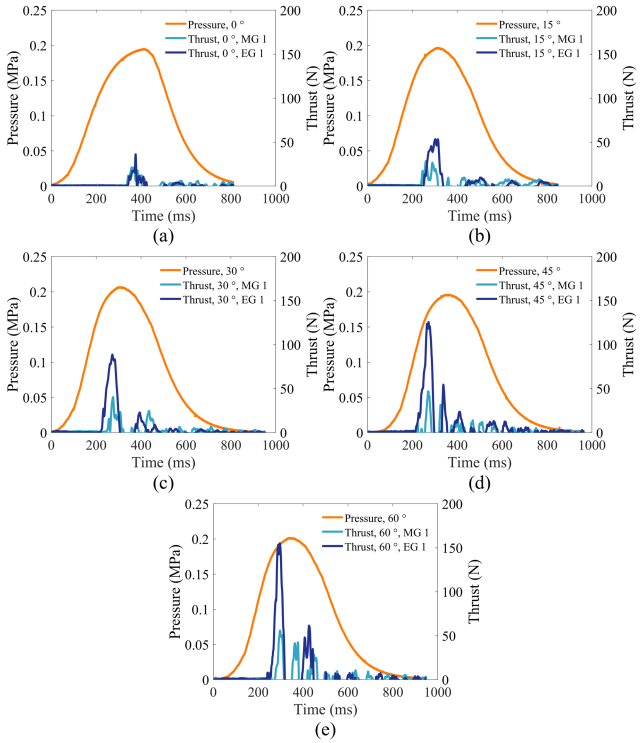

Fig. 12. Results are directly output by the pressure sensor and force sensor using thruster with C-jet structure. (a)–(e) Results for thrust and pressure over time at launch angles α of 0°, 15°, 30°, 45°, and 60°, respectively. Pressure curve represents the complete change process from inflation, to water jet, and air release. Thrust has been converted to the direction of the nozzle-axis. Thrust curve shows only positive values in each subplot. The negative values are caused by the vibration of fixed prototype under huge thrust.

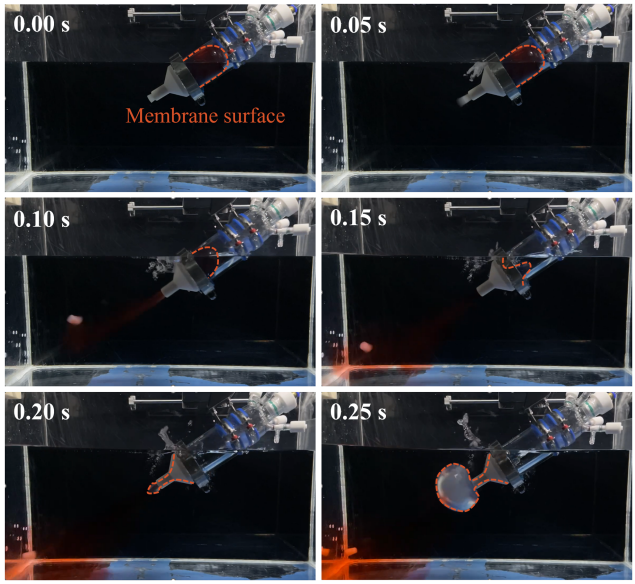

Fig. 13. Water spraying process of the thruster using CM-jet structure is recorded at 0.05 s intervals. The jetted water is precolored with a red dye, to distinguish visually. The outline of the membrane is marked with a dashed line.

growth rate of peak propulsion thrust decreases. The maximum NPT is 147 N when $\alpha = 60°$ and $P = 0.3$ MPa.

The curves of pressure and propulsion thrust with time during the jetting process are shown in Fig. 12. We chose the water-jet process when the pressure is 0.2 MPa (relative to atmospheric pressure). The propulsion curve when $\alpha = 0°$ is shown in Fig. 12(a). The propulsion curves of EG 1 and MG 1 almost coincide, which means that the thrust in this case is entirely provided by the air-jet. The peak thrust force reaches 36 N. The duration of the thrust is 76 ms. The propulsion process when $\alpha = 15°$ is shown in Fig. 12(b). The thrust curves of the EG 1 and MG 1 are clearly separated and the peak thrust was 88 N and 40 N, respectively. Both EG 1 and MG 1 sampled the second peak and the duration of the thrust was 213 ms. The propulsion curve when $\alpha = 45°$ is shown in Fig. 12(d). The third effective peak happened in EG 1 sample, and the peak propulsion forces were 123 and 46 N for the EG 1 and MG 1, respectively. The propulsion duration is 251 ms. It is clear that the magnitude and duration of propulsion are proportional to the launch angle α.

C. Propulsion Performance of CM-Jet Structure

Following the experimental setup in Sections II.B and C, the process of jetting water on the thruster using CM-jet structure is filmed in Fig. 13, and the experimental results are shown in Fig. 14. The R^2 coefficients are given in Table III and it is reasonable to consider the quadratic fit curves as the fit results. From Fig. 14(a)–(e), the numerical curves are less affected by launch angles. Each curve stays in a stable range of variation. From Fig. 14(f), the five NPT curves almost completely overlap. This is the biggest difference from the experimental results in Fig. 11(f). Besides, the peak propulsion thrust increases with increasing pressure while the rate of increase gradually decreases. The maximum NPT is 130 N when $\alpha = 30°$ and $P = 0.3$ MPa.

The pressure and thrust curves with time are shown in Fig. 15. We chose the pressure 0.2 MPa (relative to atmospheric pressure). Since the high-pressure gas cannot be discharged directly from the tail nozzle after the membrane is added, the squeezing time is shorter but the gas releasing time is longer, compared with C-jet. The time taken for the whole process is about 900 ms. The manual pressure relief takes some extra time. The propulsion processes at the five launch angles show similarity both in magnitude and in trend. The peak propulsion forces of the EG 2 at the five angles are 124, 125, 122, 127, and 130 N, and the peak propulsion forces of the MG 2 are 59, 54, 54, 59, and 60 N. The deviations of the peak propulsion forces do not exceed 6.5% and 11%, respectively.

V. Discussion

A. Effect of Membrane

The presence of membrane results in the large difference of trend (see Fig. 16). The propulsion thrust of the thruster using C-jet structure is significantly affected by the launch angle and we suppose there are two possible reasons. First, the loss of propulsion medium due to early leakage of high-pressure gas. Since the upper surface squeezed by the air cannot always

This article has been accepted for inclusion in a future issue of this journal. Content is final as presented, with the exception of pagination.

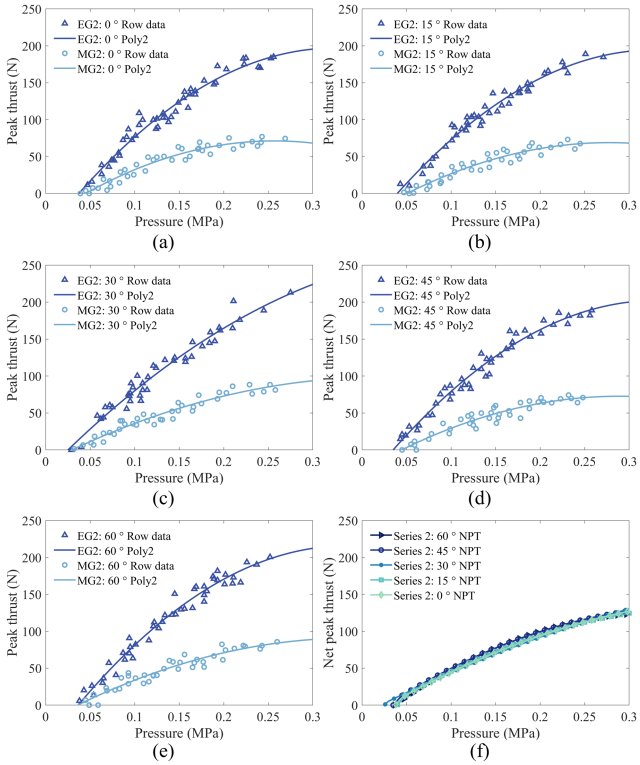

Fig. 14. Experimental results are obtained by completing experimental Series 2 using thruster with CM-jet structure. (a)–(e) Results for peak thrust and initial pressure at launch angles α of 0°, 15°, 30°, 45°, and 60°, respectively. Peak thrust has been converted to the direction of the nozzle-axis. Both the data scatter and its quadratic polynomial fit curve are shown. Each subplot shows both the results for the EG 2 and MG 2. (f) Five NPT curves are obtained by subtracting the MG 2 fit from the EG 2 fit, based on the previous five sets of fits, respectively.

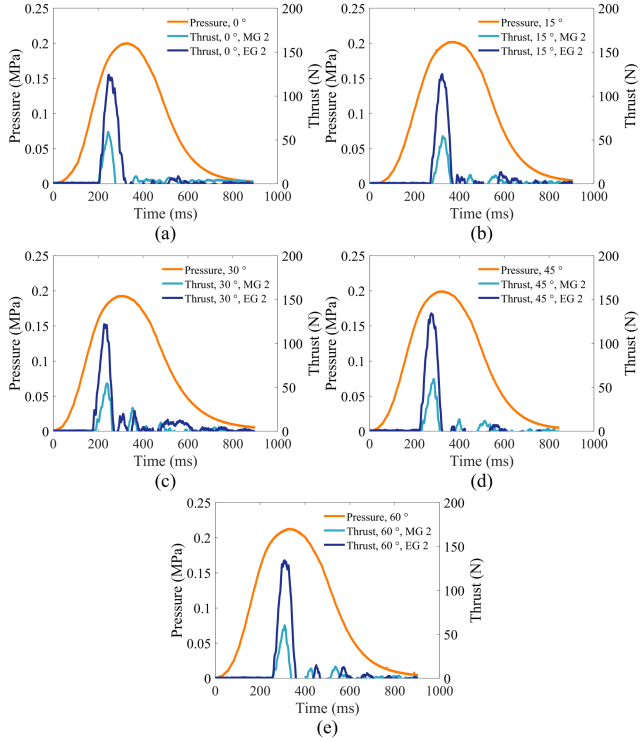

Fig. 15. Results are directly output by the pressure sensor and force sensor using thruster with CM-jet structure. (a)–(e) Results for thrust and pressure over time at launch angles α of 0°, 15°, 30°, 45°, and 60°, respectively. The pressure curve represents the complete change process from inflation, to water jet, and finally air release. The thrust has been converted to the direction of the nozzle-axis. The thrust curve shows only positive values in each subplot. The negative values are caused by the vibration of fixed prototype under huge thrust.

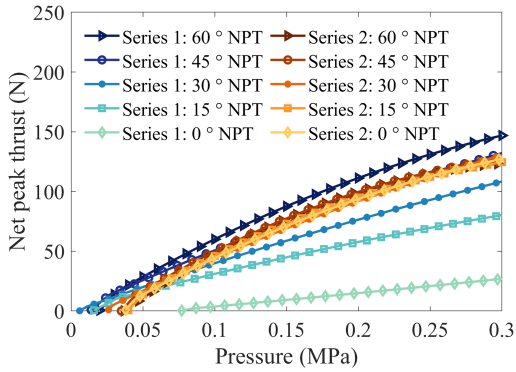

Fig. 16. Comparison of NPT curves for C-jet and CM-jet structure. The five blue ones belong to C-jet structure and five blue ones belong to CM-jet.

maintain horizontal during gas expansion, the water will be mixed with the gas and be ejected. The connected air between internal and external lead to a rapid reduction in pressure inside the prototype and the remaining water cannot be fully squeezed, which brings the waste of propulsion medium. Second, the unstable air-liquid interaction surface leads to the consumption of pressure. Due to the free flow of water, the air squeezes water like random squeezing. The pressure force on the upper surface is uniform at the beginning and tends to be released in the direction of larger downward gradient, which leads to irregular squeezing of the water and more useless work.

However, when the membrane is installed, the propulsion thrust trend exhibits consistent characteristics in CM-jet structure, which has an attitude-irrelevant propulsion stability. The effect of the launch angle is almost eliminated. The reason is that the presence of the membrane weakens the two factors mentioned above. First, the membrane isolates water and air, which allows the high-pressure gas to work entirely without leakage. The water can all be squeezed to form a jet flow without any water being left over, avoiding the waste of energy. Second, as the contact surface between water and air, the membrane makes the squeezing process more stable. The water wrapped in the membrane does not flow freely but forms an ellipsoidal shape. This shape is not distorted by random squeezing, which means that the flow of water will concentrate in the direction of tail nozzle. Those two advantages of membrane give CM-jet structure multi-directional ejection capability with huge thrust.

B. Effect of Launch Angle

The launch angle is used to reflect the propulsive difference between the two structures. The propulsive trend of the thruster

This article has been accepted for inclusion in a future issue of this journal. Content is final as presented, with the exception of pagination.

TABLE IV
COMPARISON OF THIS WORK WITH OTHER TYPICAL WATER-JET PROTOTYPES, INCLUDING UNDERWATER SOFT ROBOT (PULSATED JET PROPULSION) AND AQUAUAV

Robot type	Reference	Water-jet	Methods	Power source	Locomotion capability (translational)	Body length (mm)	Max. thrust (N)	Speed (m/s, BL/s)
Soft robot	[34]	M-jet	Tethered	Motor	1 DoF	138	10.3	0.22, 1.6
	[36]	M-jet	Tethered	Pump	1 DoF	250	1	n/a
	[37]	M-jet	Untethered	Pump	3 DoF	210	0.5	n/a
	[38]	M-jet	Tethered	Motor	1 DoF	80	1	0.16, 2
	[49]	M-jet	Tethered	Motor	2 DoF	76	n/a	0.26, 3.4
	[40]	M-jet	Tethered	Linear actuator	2 DoF	266	n/a	0.26, 0.98
AquaUAV	[18]	C-jet	Untethered	High pressure CO_2	1 DoF	n/a	5	11, n/a
	[19]	C-jet	Tethered	H_2	1 DoF	n/a	9	2.5, n/a
	[20]	C-jet	Untethered	High pressure CO_2	1 DoF	790	n/a	0.5, n/a
	[23]	C-jet	Untethered	C_2H_2	1 DoF	n/a	43	10, n/a
	This work	CM-jet	Tethered	High pressure gas	3 DoF	365	130	n/a

The DoF of locomotion capabilities here are described in a Cartesian coordinate system. 1 DoF means the prototype can only move along a straight line. 2 DoF means the prototype can move in a specific plane. 3 DoF means the prototype can move in three dimensions.

using C-jet structure is most significantly affected by the launch angle, while the thruster using CM-jet is not. When the launch angle is small, the high-pressure gas in the thruster using C-jet structure is more likely to escape from the tail nozzle. More water is left over, which results in less propulsion momentum. The high-pressure gas realizes piston-like squeezing and the water are ejected more directly and effectively in the C-jet structure when the launch angle becomes larger, while there is loss of energy transfer in the CM-jet structure because of the membrane deformation. This explains why the thrust curve of C-jet structure is higher than that of the CM-jet at larger launch angle. The stable propulsion of the CM-jet structure is equivalent to the propulsive performance of the C-jet at 45° launch angle (see Fig. 16). That means thruster with CM-jet structure have omnidirectional accelerating capability, as excellent as traditional thruster with C-jet at 45° launch angle (parabolic trajectories can reach the highest and farthest).

C. Effect of Initial Pressure

The trend of propulsion thrust with pressure is fitted with the quadratic polynomial, which is consistent for the two structures. All curves show the trend of rising first and then entering plateau period (see Fig. 16). The slope of trends becomes smaller, which gradually occur between 0.2 and 0.4 MPa follow the prediction of Section III. This is because the larger the initial pressure, the faster the velocity of water flow and the greater the viscous losses, as discussed in (11) and (12). If we want to obtain greater propulsion under greater pressure, the internal flow field structure and inner wall roughness of the thruster must be optimized.

D. Model Interpretation

There are some points in Section III.B and Section III.C need to be explained and corrected. First, the upper level of the water is not always consistent during the jetting process (see Fig. 10). It changes from horizontal to inclined, which means that the internal gas is connected to the outside with the inclined liquid level, leading to leakage. This is especially noticeable after 0.2 s. Since the contact area S_i and dropping distance d_i satisfy $S_i d_i = V_{w_i}$, using V_{w_i} will eliminate this effect on model predictions. Second, the two original settings in the model, waste of propulsion medium and early leakage of pressure, are consistent with the experimental phenomenon (see Figs. 10 and 13). A large number of white bubbles are ejected at 0.3 s, which means that the internal high pressure is leaked. However, the ejected color becomes red again after 0.4 s, meaning that the remaining reddened water inside the prototype is ejected by the airflow although no additional propulsion is generated. For CM-jet structure, the predicted membrane deformation process matches the reality (see Figs. 7 and 13). The deformation of the ellipsoidal membrane is fixed in the short-axis plane and varies in the long-axis. Besides, the elasticity of the membrane has a minor effect on the propulsion thrust. Due to the elastic potential energy stored in the deformation, the water wrapped in the membrane are slowly ejected from the tail nozzle without gas extrusion. The force collected by the force sensor is small (less than 3 N), which can be ignored for the model predictions and propulsion tends.

E. Future Work

Currently we can quantitatively compare the two water-jet structures using the same prototype, TGTS. It presents the C-jet structure when there is no membrane and the CM-jet structure when there is a membrane. However, the experimental platform can indeed be further improved. If we optimize the clamping between the TGTS and the membrane, the airtightness can be better. Currently, the TGTS leaks (given in the supplementary materials) when the pressure is too high (more than 0.4 MPa). In the future, we will miniaturize the water-jet thruster of CM-jet structure with integrated power and communication.

Table IV compares this work with other robotic prototypes that use water-jet thruster, such as underwater soft robot and AquaUAV. Our work is the only one that uses CM-jet structure as thruster. For locomotion capability, our new proposed CM-jet structure is independent of the launch angle. It has a stable propulsive performance regardless of the initial attitude in the

This article has been accepted for inclusion in a future issue of this journal. Content is final as presented, with the exception of pagination.

horizontal and vertical planes, which means thruster will handle three translational DoF in three dimensions with the help of the rudder. And the maximum thrust is much larger than other works.

VI. Conclusion

We developed a novel water-jet structure, the CM-jet structure. A tethered prototype and force-pressure measurement system are built. We designed two experimental series here to compare the propulsion performance of thrusters using C-jet and CM-jet structure. Based on the observed experimental phenomena, theoretical models of those two structures are constructed. The thruster using CM-jet structure generates steady propulsion properties unrelated to attitude when the launch angle is changed, and C-jet structure shows dispersion that the propulsion performance varies greatly with launch angles. The larger the launch angle, the higher the propulsion thrust curve. The stable propulsion of the CM-jet structure is equivalent to the propulsive performance of the C-jet at 45° launch angle, and the maximum NPT reaches 130 N. The former is larger when the launch angle $\alpha < 45°$ and the latter is larger when $\alpha > 45°$.

Fast water-jet propulsion can be used as an acceleration method during the underwater cruising. The attitude-irrelevant propulsion generated by the thruster using CM-jet structure may be able to broaden the direction of water-jet acceleration, making it even omnidirectional. It helps the prototype to achieve fast locomotion in three translational DoF with more thrust than propeller.

References

[1] K. Cole and D. Gilbert, "Jet propulsion of squid," *Biol. Bull.*, vol. 138, no. 3, pp. 245–246, 1970.

[2] A. Packard, "Cephalopods and fish: The limits of convergence," *Biol. Rev.*, vol. 47, no. 2, pp. 241–307, 1972.

[3] E. J. Anderson and M. E. DeMont, "The mechanics of locomotion in the squid Loligo Pealei: Locomotory function and unsteady hydrodynamics of the jet and intramantle pressure," *J. Exp. Biol.*, vol. 203, no. 18, pp. 2851–2863, 2000.

[4] R. O'Dor, J. Stewart, W. Gilly, J. Payne, T. C. Borges, and T. Thys, "Squid rocket science: How squid launch into air," *Deep Sea Res. Part II: Topical Stud. Oceanogr.*, vol. 95, pp. 113–118, 2013.

[5] J. M. Gosline and M. E. DeMont, "Jet-propelled swimming in squids," *Sci. Amer.*, vol. 252, no. 1, pp. 96–103, 1985.

[6] R. O'Dor, "How squid swim and fly," *Can. J. Zool.*, vol. 91, no. 6, pp. 413–419, 2013.

[7] B. J. Gemmell et al., "Passive energy recapture in jellyfish contributes to propulsive advantage over other metazoans," *Proc. Nat. Acad. Sci.*, vol. 110, no. 44, pp. 17904–17909, 2013.

[8] H. E. Guderley and I. Tremblay, "Escape responses by jet propulsion in scallops," *Can. J. Zool.*, vol. 91, no. 6, pp. 420–430, 2013.

[9] R. O'dor and D. Webber, "Invertebrate athletes: Trade-offs between transport efficiency and power density in cephalopod evolution," *J. Exp. Biol.*, vol. 160, no. 1, pp. 93–112, 1991.

[10] J. O. Dabiri, "Optimal vortex formation as a unifying principle in biological propulsion," *Annu. Rev. Fluid Mech.*, vol. 41, pp. 17–33, 2009.

[11] R. Siddall and M. Kovač, "Launching the aquamav: Bioinspired design for aerial–aquatic robotic platforms," *Bioinspiration Biomimetics*, vol. 9, no. 3, 2014, Art. no. 031001.

[12] X. Yang, T. Wang, J. Liang, G. Yao, and M. Liu, "Survey on the novel hybrid aquatic–aerial amphibious aircraft: Aquatic unmanned aerial vehicle (AQUAUAV)," *Prog. Aerosp. Sci.*, vol. 74, pp. 131–151, 2015.

[13] X. Wang et al., "Aquatic unmanned aerial vehicles (AQUAUAV): Bionic prototypes, key technologies, analysis methods, and potential solutions," *Sci. China Technological Sci.*, vol. 66, no. 8, pp. 2308–2331, 2023.

[14] T. Wang, X. Yang, J. Liang, G. Yao, and W. Zhao, "CFD based investigation on the impact acceleration when a gannet impacts with water during plunge diving," *Bioinspiration Biomimetics*, vol. 8, no. 3, 2013, Art. no. 036006.

[15] J. Liang, X. Yang, T. Wang, G. Yao, and W. Zhao, "Design and experiment of a bionic gannet for plunge-diving," *J. Bionic Eng.*, vol. 10, no. 3, pp. 282–291, 2013.

[16] W. Stewart et al., "Design and demonstration of a seabird-inspired fixed-wing hybrid UAV-UUV system," *Bioinspiration biomimetics*, vol. 13, no. 5, 2018, Art. no. 056013.

[17] D. Lu et al., "Design, fabrication, and characterization of a multimodal hybrid aerial underwater vehicle," *Ocean Eng.*, vol. 219, 2021, Art. no. 108324.

[18] R. Siddall and M. Kovač, "A water jet thruster for an aquatic micro air vehicle," in *Proc. IEEE Int. Conf. Robot. Autom.*, 2015, pp. 3979–3985.

[19] Y. Chen et al., "A biologically inspired, flapping-wing, hybrid aerial-aquatic microrobot," *Sci. Robot.*, vol. 2, no. 11, 2017, Art. no. eaao5619.

[20] T. Hou et al., "Design and experiments of a squid-like aquatic-aerial vehicle with soft morphing fins and arms," in *Proc. Int. Conf. Robot. Autom.*, 2019, pp. 4681–4687.

[21] T. Hou et al., "Design, fabrication and morphing mechanism of soft fins and arms of a squid-like aquatic-aerial vehicle with morphology tradeoff," in *Proc. IEEE Int. Conf. Robot. Biomimetics*, 2019, pp. 1020–1026.

[22] T. Hou, X. Yang, T. Wang, J. Liang, S. Li, and Y. Fan, "Locomotor transition: How squid Jet from water to air," *Bioinspiration Biomimetics*, vol. 15, no. 3, 2020, Art. no. 036014.

[23] R. Zufferey et al., "Consecutive aquatic jump-gliding with water-reactive fuel," *Sci. Robot.*, vol. 4, no. 34, 2019, Art. no. eaax7330.

[24] R. Siddall, G. Kennedy, and M. Kovac, "High-power propulsion strategies for aquatic take-off in robotics," in *Robotics Research*. Cham, Switzerland: Springer, 2018, pp. 5–20.

[25] J. O. Dabiri, S. Colin, K. Katija, and J. H. Costello, "A wake-based correlate of swimming performance and foraging behavior in seven co-occurring jellyfish species," *J. Exp. Biol.*, vol. 213, no. 8, pp. 1217–1225, 2010.

[26] N. W. Xu, "Squid-inspired robots perform swimmingly," *Sci. Robot.*, vol. 6, no. 50, 2021, Art. no. eabf4301.

[27] R. Wang, S. Wang, Y. Wang, L. Cheng, and M. Tan, "Development and motion control of biomimetic underwater robots: A survey," *IEEE Trans. Syst., Man, Cybern. Syst.*, vol. 52, no. 2, pp. 833–844, Feb. 2022.

[28] X. Wang, X. Pei, X. Wang, and T. Hou, "Bionic robot manta ray based on dielectric elastomer actuator," in *Proc. IEEE Int. Conf. Front. Robot. Softw. Eng.*, 2023, pp. 387–392.

[29] J. Zhu, C. White, D. K. Wainwright, V. Di Santo, G. V. Lauder, and H. Bart-Smith, "Tuna robotics: A high-frequency experimental platform exploring the performance space of swimming fishes," *Sci. Robot.*, vol. 4, no. 34, 2019, Art. no. eaax4615.

[30] D. Chen, Z. Wu, Y. Meng, M. Tan, and J. Yu, "Development of a high-speed swimming robot with the capability of fish-like leaping," *IEEE/ASME Trans. Mechatronics*, vol. 27, no. 5, pp. 3579–3589, 2022.

[31] T. Li et al., "Fast-moving soft electronic fish," *Sci. Adv.*, vol. 3, no. 4, 2017, Art. no. e1602045.

[32] Y. Meng, Z. Wu, P. Zhang, J. Wang, and J. Yu, "Real-time digital video stabilization of bioinspired robotic fish using estimation-and-prediction framework," *IEEE/ASME Trans. Mechatronics*, vol. 27, no. 6, pp. 4281–4292, Dec. 2022.

[33] M. Krieg and K. Mohseni, "Dynamic modeling and control of biologically inspired vortex ring thrusters for underwater robot locomotion," *IEEE Trans. Robot.*, vol. 26, no. 3, pp. 542–554, Jun. 2010.

[34] F. Renda, F. Giorgio-Serchi, F. Boyer, and C. Laschi, "Modelling cephalopod-inspired pulsed-jet locomotion for underwater soft robots," *Bioinspiration biomimetics*, vol. 10, no. 5, 2015, Art. no. 055005.

[35] F. Giorgio-Serchi, A. Arienti, and C. Laschi, "Underwater soft-bodied pulsed-jet thrusters: Actuator modeling and performance profiling," *Int. J. Robot. Res.*, vol. 35, no. 11, pp. 1308–1329, 2016.

[36] F. Giorgio-Serchi, A. K. Lidtke, and G. D. Weymouth, "A soft aquatic actuator for unsteady peak power amplification," *IEEE/ASME Trans. Mechatronics*, vol. 23, no. 6, pp. 2968–2973, Dec. 2018.

[37] J. Frame, N. Lopez, O. Curet, and E. D. Engeberg, "Thrust force characterization of free-swimming soft robotic jellyfish," *Bioinspiration Biomimetics*, vol. 13, no. 6, 2018, Art. no. 064001.

[38] M. A. Robertson, F. Efremov, and J. Paik, "Roboscallop: A bivalve inspired swimming robot," *IEEE Robot. Autom. Lett.*, vol. 4, no. 2, pp. 2078–2085, Apr. 2019.

[39] C. J. Gommes, "A more thorough analysis of water rockets: Moist adiabats, transient flows, and inertial forces in a soda bottle," *Amer. J. Phys.*, vol. 78, no. 3, pp. 236–243, 2010.

This article has been accepted for inclusion in a future issue of this journal. Content is final as presented, with the exception of pagination.

[40] T. Bujard, F. Giorgio-Serchi, and G. D. Weymouth, "A resonant squid-inspired robot unlocks biological propulsive efficiency," *Sci. Robot.*, vol. 6, no. 50, 2021, Art. no. eabd2971.
[41] F. Giorgio-Serchi and G. Weymouth, "Drag cancellation by added-mass pumping," *J. Fluid Mech.*, vol. 798, p. R3, 2016. [Online]. Available: https://www.cambridge.org/core/journals/journal-of-fluid-mechanics/article/abs/drag-cancellation-by-addedmass-pumping/95A2F2919472B06287CF9ECC00E704C5
[42] X. Bi and Q. Zhu, "Dynamics of a squid-inspired swimmer in free swimming," *Bioinspiration Biomimetics*, vol. 15, no. 1, 2019, Art. no. 016005.
[43] G. D. Weymouth and F. Giorgio-Serchi, "Analytic modeling of a size-changing swimmer," in *Advances in Critical Flow Dynamics Involving Moving/Deformable Structures With Design Applications*. Cham, Switzerland: Springer, 2021, pp. 585–595.
[44] J. Wu, X. Wang, X. Pei, and T. Hou, "Design and simulation analysis of mantle cavity of jet thruster," in *Proc. IEEE Int. Conf. Front. Robot. Softw. Eng.*, 2023, pp. 347–354.
[45] F. G. Serchi, A. Arienti, and C. Laschi, "Biomimetic vortex propulsion: Toward the new paradigm of soft unmanned underwater vehicles," *IEEE/ASME Trans. On Mechatronics*, vol. 18, no. 2, pp. 484–493, Apr. 2013.
[46] G. Weymouth, V. Subramaniam, and M. Triantafyllou, "Ultra-fast escape maneuver of an octopus-inspired robot," *Bioinspiration Biomimetics*, vol. 10, no. 1, 2015, Art. no. 016016.
[47] F. Giorgio-Serchi and G. D. Weymouth, "Underwater soft robotics, the benefit of body-shape variations in aquatic propulsion," in *Soft Robotics: Trends, Applications and Challenges*. Cham, Switzerland: Springer, 2017, pp. 37–46.
[48] R. Siddall and M. Kovac, "Fast aquatic escape with a jet thruster," *IEEE/ASME Trans. Mechatronics*, vol. 22, no. 1, pp. 217–226, Feb. 2017.
[49] Y. Wang et al., "Development of a biomimetic scallop robot capable of jet propulsion," *Bioinspiration Biomimetics*, vol. 15, no. 3, 2020, Art. no. 036008.

Xinyang Wang is currently working toward the B.E. degree in mechanical engineering with the School of Mechanical Engineering and Automation, Beihang University, Beijing, China.

His research focuses on bioinspired robotics and its applications.

Xuan Pei received the B.E. degree from the School of Mechanical Engineering, Hefei University of Technology, Hefei, China, in 2017, and the M.E. degree in mechanical engineering from the School of Mechanical Engineering and Automation, Beihang University, Beijing, China, in 2020.

His research interests include robotics, machine learning, and its application.

Ruixiang Zhu received the B.E. degree in automation from Anhui University, Hefei, China, in 2019. She is currently working toward the M.S. degree in traffic information engineering and control with the School of Electronic and Information Engineering, Beijing Jiaotong University, Beijing, China.

Her research interests include intelligent robotics and UAV landing control.

Taogang Hou received the B.E. and Ph.D. degrees in mechanical engineering from Beihang University, Beijing, China, in 2016 and 2020, respectively.

He is currently an Associate Professor with the School of Electronic and Information Engineering, Beijing Jiaotong University, Beijing. His research interests include intelligent robotics, visual perception under high-speed movement, and smart transportation system.

Xingbang Yang received the B.E. degree and Ph.D. degree in mechanical engineering from the School of Mechanical Engineering and Automation, Beihang University, Beijing, China.

He is currently an Associate Professor with the School of Biological Science and Medical Engineering, Beihang University, Beijing. His current research interests include bioinspired robotics, exoskeleton robotics, and prosthetics.